J. Fluid Mech. (1981), *vol.* 107, *pp.* 173–200
Printed in Great Britain

Direct measurement of vorticity by optical probe

By MICHAEL B. FRISH AND WATT W. WEBB
School of Applied and Engineering Physics, Cornell University, Ithaca, N.Y. 14853

(Received 12 April 1980)

An optical method for the direct measurement of vorticity in liquid flows is described. At the present state of development it is capable of responding to vorticity fluctuations with a response time of about 1 msec and a spatial resolution of better than 50 μm. Small spherical particles suspended in the flow rotate with angular velocity accurately equal to half the local vorticity; thus measurements of the rotation rates of such particles indicate the vorticity. Transparent spherical particles of less than 50 μm diameter, each containing embedded planar crystal mirrors, have been developed for this purpose and are suspended in a refractive-index-matched liquid. Measurements of the times required for laser reflections from the mirrors to rotate through the small angle defined by a pair of slits yields the rotation rate, and thus the vorticity. Production and physical properties of the probe particles are reported. Theoretical capabilities and limitations of the method, including accuracy, spatial and temporal resolution, data rate, and background noise are calculated and found to be coupled to the optical geometry and flow field. Analysis yields procedures for selective optimization of each parameter as dictated by the particular application. Measurements of steady-state, laminar, two-dimensional Poiseuille flows demonstrate the effectiveness of the technique and confirm theoretical predictions.

1. Introduction

Although the vorticity field, $\boldsymbol{\omega}(\mathbf{x},t) = \nabla \times \mathbf{v}(\mathbf{x},t)$, is an essential property of rotational and turbulent flow, requisite measurements of the vorticity transcend experimental capability. Modern techniques of hot-wire and hot-film anemometry and laser-Doppler anemometry can measure components of the velocity field $\mathbf{v}(\mathbf{x},t)$ at a limited number of points. The velocity components are ordinarily analysed by finite differences or application of Taylor's frozen-flow hypothesis to calculate the vorticity (see, for example, Eckelmann *et al.* 1977; Foss 1977; Willmarth & Bogar 1977), but error magnification by the necessary differentiations limits the accuracy and spectral range. Spatial resolution of the method has usually been limited to about 0·1 cm by hot-wire probe geometry although Willmarth & Bogar (1977) have recently reported a spatial resolution of 100 μm. In principle flow perturbations can be avoided and the spatial resolution can be slightly improved by laser-Doppler anemometry but the complexity of these simultaneous optical measurements has apparently deterred its application to vorticity measurement.

The ideal system for vorticity measurement should meet these criteria: Spatial resolution exceeding the inner scale of turbulence η ($\eta \sim 50\,\mu$m in common liquid flows), temporal resolution exceeding the shortest expected vorticity fluctuation time,

and data acquisition rates, spectral range and measurement accuracy sufficient for calculation of vorticity correlation functions and higher moments of vorticity.

The potential of such measurements of vorticity has motivated a disparate approach to this difficult measurement problem. Encouraged by the successful development of a method of optical scattering from anisotropic, submicroscopic particles for direct measurement of the strain-rate tensor with excellent spatial resolution (Johnson & Webb 1972), a new optical method for direct measurement of vorticity distributions in liquids with 50 μm spatial resolution has been developed and is described here. It is based on the propensity of small spherical particles suspended in flowing fluid to accurately track the local vorticity $\boldsymbol{\omega}$ by rotation with angular velocity $\boldsymbol{\Omega} = \frac{1}{2}\boldsymbol{\omega}$. Reflections from a dispersion of small transparent plastic spheres each containing one or more flat, highly reflecting mirrors provide the desired indicator of local vorticity. To measure vorticity, a few volume per cent of these particles are added to a transparent liquid of matching refractive index. A laser beam illuminating a small volume of the flow to be sampled is reflected by the rotating particles. The rotational velocity of each reflected beam, which equals the local vorticity at the reflecting particle, is measured by observing the transit time of the reflected beam across a small angle defined by a pair of closely spaced slits. Each such transit provides a datum for prompt on-line calculation of the instantaneous local vorticity that is stored for analysis of the vorticity distribution. This measurement system is here called the vorticity optical probe or VOP for brevity.

The vorticity measurement system is described in § 2 of this paper. There the processs of manufacture and the physical properties of the probe particles are reported in some detail. This is followed by a description of the data collection system designed for application to laboratory scale wakes, mixing layers and boundary layers in channels at modest Reynolds numbers. The characteristics of the detected reflexions, which tend to limit the precision of the technique, depend on both reflecting particle properties and optical-system geometry. The optical geometry its and effect on measurement performance are discussed and the signal acquisition and data-processing procedure are described.

Section 3 presents a theoretical discussion of basic experimental capabilities and limitations of the method including accuracy, spatial and temporal resolution, data rate and background noise, and their dependence on experimental parameters. To describe how the interplay of inhomogeneity of flow with the optical geometry and the optical imperfections limits the available vorticity measurement resolution a system-resolution function is defined.

Section 4 describes experimental tests of the measurement system by application to steady-state Poiseuille flows. Measured vorticity distributions confirm theoretical expectations and demonstrate the effectiveness of the vorticity optical probe.

Finally in § 5 the properties of the vorticity optical probe system are summarized and prospects for applications and future development are discussed.

2. Vorticity measurement system

2.1. *Fundamental concepts*

The vorticity measurement system comprises: (1) the spherical probe particles containing planar mirrors; (2) refractive-index-matched fluid; (3) optical system; (4) data acquisition and analysis system.

Each aspect of the system will be discussed in turn. First, however, the fundamental hypothesis that small spherical particles follow the flow must be established.

Chwang & Wu (1974) have calculated the couple due to local vorticity acting on small particles of various shapes with results that agree with the early calculation of Jeffrey (1922) for spheroids. Application of their results shows that the spherical probe particles faithfully follow flow fluctuations that occur on a time scale slower than about 1 ms. The calculations are valid when the Reynolds number based on particle radius r and velocity u relative to the surrounding fluid is much less than unity. Stokes' law suggests that relative velocity will relax exponentially with relaxation time

$$\tau_u = \tfrac{2}{9} r^2 \rho / \mu, \tag{2.1}$$

where r is the sphere radius, ρ the particle density, and μ the dynamic viscosity. With appropriate data for the probe particles, $\rho = 1{\cdot}2\,\mathrm{g\,cm^{-3}}$, $\mu = 0{\cdot}005\,\mathrm{g\,cm^{-1}\,s^{-1}}$ and $r = 25 \times 10^{-4}\,\mathrm{cm}$, the relative velocity relaxation time is $\tau_u \sim 0{\cdot}4\,\mathrm{ms}$. Hence, the calculation of Chwang & Wu is valid for the probe particles for time scales $\gtrsim 1\,\mathrm{ms}$.

Chwang & Wu's equation (11) gives the torque on a sphere of radius r rotating at angular velocity Ω relative to the surrounding fluid as $M = -8\pi\mu r^3\Omega$. Thus the relative rotational relaxation time is

$$\tau_r = \tfrac{1}{15} r^2 \rho / \mu. \tag{2.2}$$

For the probe particles $\tau_r \sim 0{\cdot}1\,\mathrm{ms}$.

The shortest time scale in turbulent flow is the Kolmogorov micro-scale of time (Tennekes & Lumley 1972)

$$\tau_k \sim (l/u)\, R_l^{-\frac{1}{2}}, \tag{2.3}$$

where R_l is the turbulence Reynolds number, l the integral length scale, and u the turbulent velocity. Extreme values in laboratory water tunnel flows are $l \sim 0{\cdot}3\,\mathrm{cm}$, $u \sim 7\,\mathrm{cm\,s^{-1}}$, and $R_l \sim 200$ (Frenkiel, Klebanoff & Huang 1979), giving $\tau_k = 3\,\mathrm{ms}$. Therefore the probe particles should readily follow rotational and translational fluctuations in anticipated turbulent liquid flows.

This line of analysis also provides, following Jeffrey (1922), an estimate of the possible measurement error due to non-spherical particles that might be formed by damage or adhesion of spherical probe particles. Non-spherical particles do not rotate with the same angular velocity as the fluid. Their long axes tends to align with the principal strain rate in a non-uniform flow. Approximating an adherent pair of spheres by an ellipsoid of major axis $4r$ yields a variable rotation rate of the form

$$\Omega_p = \frac{4}{5} \frac{dv/dy}{1 + 3\sin^2[\frac{2}{5}(dv/dy)\,t]}, \tag{2.4}$$

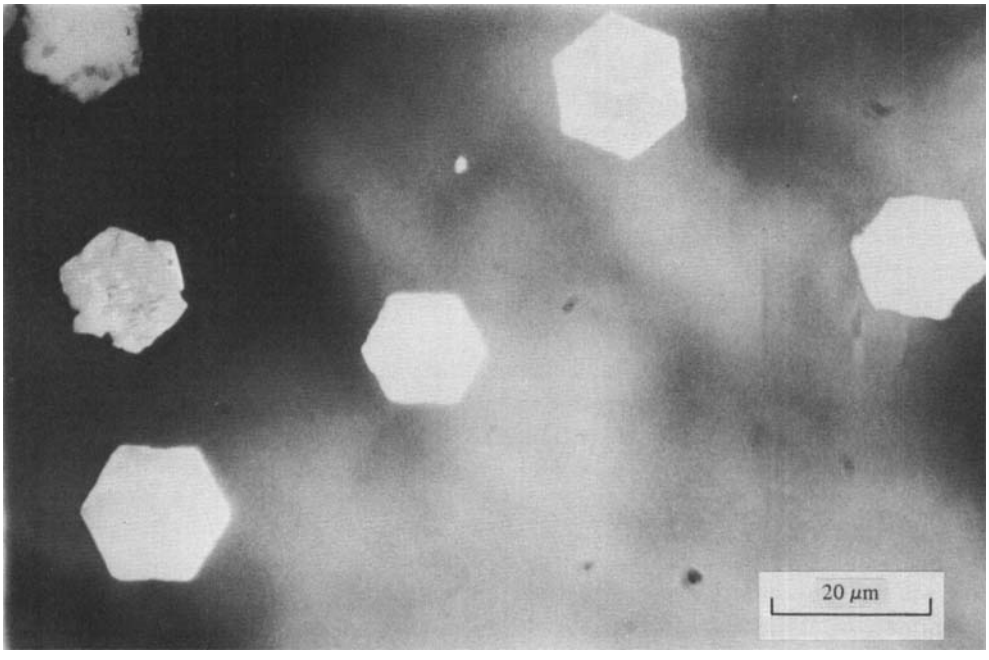

FIGURE 1. Photomicrograph of basic lead carbonate crystals in reflected light.

where dv/dy is the maximum magnitude of the local velocity gradient. The rotation rate Ω_p of this ellipsoid varies from the rate Ω for spherical particles within the limited range

$$\tfrac{2}{5}\Omega < \Omega_p < \tfrac{8}{5}\Omega. \tag{2.5}$$

Thus defective probe particles would contribute a broadened background to vorticity measurements.

Rotation of the probe spheres should not be perturbed by inter-particle interaction and they should not perturb the fluid flow. Jeffrey (1922) showed that the effective viscosity of the bulk fluid will be increased by a factor of $1 + 2{\cdot}5V$ by the addition of a volume fraction V of solid spherical particles. Thus the probe particle number density n should be limited so that the volume fraction of particles is small, that is $\frac{4}{3}\pi r^3 n \ll 1$. For spheres of $25\,\mu$m radius this requires $n \ll 1{\cdot}5 \times 10^7\ \mathrm{cm}^{-3}$. A more-than-ample concentration, 10^6 particles cm^{-3}, increases the viscosity by only 10 %.

2.2. *Probe particles*

The preceding section indicates that spherical particles of radius $r \lesssim 25\,\mu$m and moderate density accurately sample the local vorticity. They rotate at an angular velocity Ω equal to half the local vorticity ω (Batchelor 1967, §§2.3, 2.4). Uniform dispersion of the particles requires that they not stick together and that the particle density approximate that of the fluid. To minimize light scattering the refractive index of the particles must closely match that of the fluid. The essential development enabling this optical method for vorticity measurement is the process for production of large quantities of transparent spherical particles containing planar mirrors. The

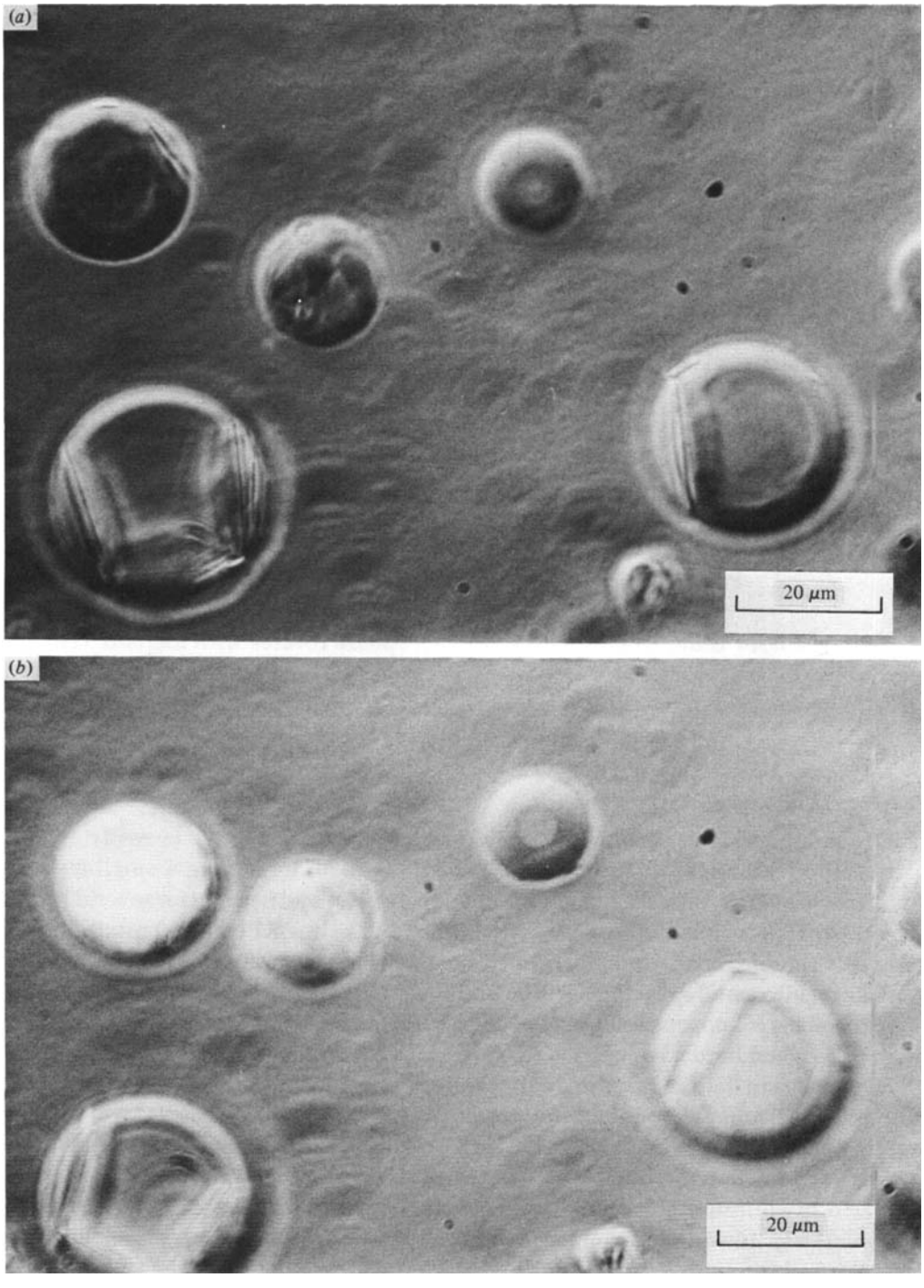

FIGURE 2. Photomicrograph of spherical plastic particles with embedded lead carbonate crystal 'mirrors', in index-matching fluid, by phase-contrast microscopy. (*a*) Transmitted light; (*b*) reflected light.

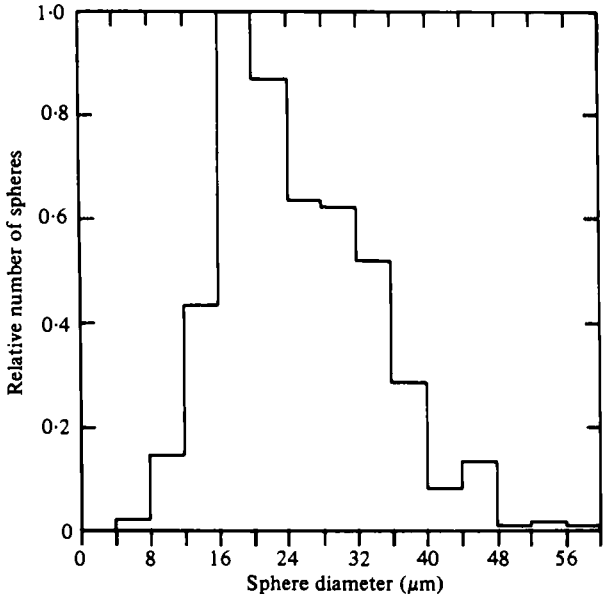

FIGURE 3. Histogram of particle diameter distribution.

reflexion of a laser beam from a mirror-bearing sphere rotates with angular velocity equal to the local vorticity ω.

The following subsections describe the manufacture and characteristics of the probe particles.

(*a*) *Particle manufacture*

Methylmethacrylate monomer, a volatile, low-viscosity liquid, is easily 'mass' polymerized (Rodriguez 1970: Redfarn & Bedford 1960) by adding a small amount (0·1% by weight) of initiator (usually benzoyl peroxide) and heating for several hours. A clear, hard, plastic solid (commercially known as Lucite or Plexiglas) results. If the non-water-soluble monomer is suspended in a continuously stirred aqueous solution, it breaks up into small spherical 'pearls' and the same chemical polymerization occurs. This procedure is known as suspension or pearl polymerization since the pearls retain their shape when hardened.

The suspension fluid consists of 2 g/l polyvinyl alcohol (PVA), 1·5 g/l each of sodium chloride (NaCl) and ammonium thiocyanate (NH_4SCN) in doubly distilled water. PVA prevents the liquid pearls from coalescing once they are separated, NaCl helps to prevent partially polymerized pearls from sticking together, and NH_4SCN inhibits the formation of emulsion polymer (Rodriguez 1970; Hopff, Lüssi & Gerspacher 1964). Approximately 150 ml of monomer plus initiator is added to 850 ml of solution, and then whipped for 5 s in a Montgomery Ward pulse action blender. The suspension is then poured into a one-litre volumetric flask, heated to 65–70 °C and magnetically stirred on a Corning heater/stirrer for about five hours. The spheres harden and, when, dried form about 100 ml of slippery powder.

Lead carbonate 'mirrors' are easily incorporated in the particles before they

polymerize by adding 7·5 ml of Mearlmaid Nacromer ZTX-B (supplied by Mearl Co.) to the monomer before whipping. The mirrors are hexagonal platelets with widths of 8–30 μm, thickness of 0·07 μm and refractive index of 2·2 (see figure 1). The mirrors generally remain fully enclosed by the plastic spheres throughout the process and do not interfere with the polymerization chemistry.

(*b*) *Particle characteristics*

The resulting spheres have a density of about 1·2 g cm^{-3} and a refractive index of 1·49. Microscopy shows a diameter range of about 5–200 μm. The smallest spheres contain no mirrors, the larger ones contain several. Since only spheres smaller than a Kolmogorov microscale (Tennekes & Lumley 1972) of roughly 50 μm that contain mirrors are desired, gravitational sedimentation (Cadle 1955) is used to narrow the size range. Figures 2 (*a*, *b*) show phase-contrast photomicrographs of finished particles imbedded in an index-matching fluid and illuminated by transmitted and reflected light respectively. Measurements of many similar pictures determined the final particle diameter distribution shown in figure 3. The average diameter is 21 μm. It appears that there are on the average about two mirrors per sphere.

To check for flocculation and non-spherical or otherwise defective particles a microscopic flow system was constructed in which the particles could be observed under actual flow conditions. It was found that a small minimum shear rate, which is easily surpassed in any laboratory flow system, sufficed to keep the spheres dispersed. The observations also show that approximately 3 % of the particles have defects such as fractures or non-spherical form. An additional 3–4 % appear to be stuck together in inseparable pairs or occasional triplets.

2.3. *Fluid selection*

The particles must be suspended in a fluid having the following properties: (1) refractive index which nearly matches that of the spheres (1.49) to prevent scattering from their surfaces that would limit the optical depth; (2) no dissolution or chemical reactivity with the particles or components of the flow system; (3) density near that of the particles to prevent rapid settling out; (4) low viscosity to facilitate experiments with high Reynolds number; (5) non-foaming surface properties; (6) low vapour pressure, toxicity and flammability for safety and convenience; and (7) low cost to permit economical extension to large-scale apparatus.

Two fluids, dibutyl phthalate and *p*-cymene, were found which satisfy all or most of the requirements. The former has a viscosity of 0·15 g cm^{-1} s^{-1} which is suitable for the laminar flow experiments, while the latter has lower viscosity, 0·005 g cm^{-1} s^{-1}, but somewhat higher flammability and vapour pressure. Certain concentrated solutions of salts in water that also satisfy most of these critera are excessively corrosive.

2.4. *Detection system*

The detection system consists of two parts, the optical system and the electronics for data collection and processing. The optical system is designed to perform two functions: Define the sampled volume in the fluid, and define the particle rotation angle to be timed by the electronics. The sampled volume is defined by the illuminating laser beam and a lens–slit combination that collects the reflections and limits the observed

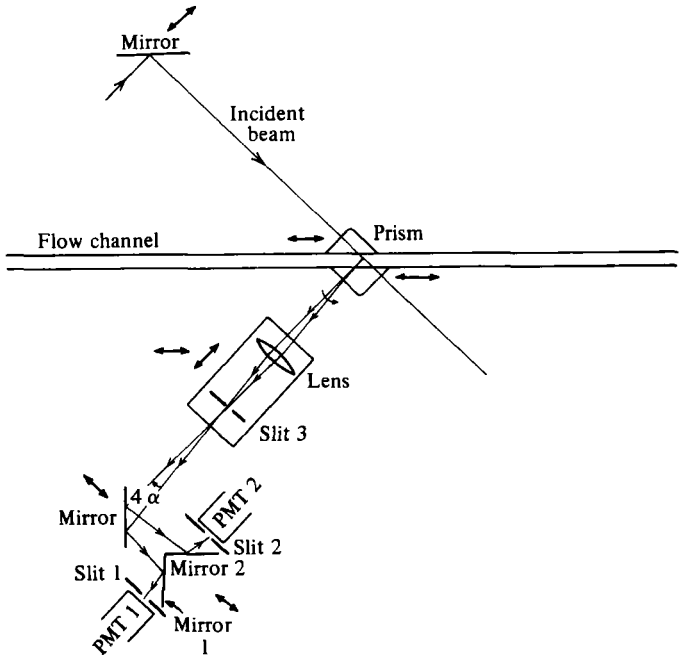

FIGURE 4. Optical detection system.

length of the laser beam as will be described. Another pair of slits with fixed separation defines the rotation angle. Light passing through these slits is converted to electrical pulses by photomultipliers (RCA 7265). The pulses trigger a pair of threshold detectors, one of which (*on*) starts a clock on a pulse from the first PMT and the second (*off*) stops the clock on a pulse from the second PMT. The elapsed time is read by a computer which immediately calculates the vorticity. The accuracy of the data is determined by the regularity of the light beams passing through the slits, which in turn is determined by the quality of the reflexions from the particles and the quality of the optical components. In this section the detection system is described in detail to provide a basis for a determination of the measurement uncertainty function.

(*a*) *Optical system*

(i) *Optical system geometry*. Figure 4 shows a schematic diagram of the optical system and its relationship to the flow system. The incident beam enters the channel at a 45° angle through a prism which is refractive-index-matched to the channel wall. The reflexions from suitably oriented particles emerge nearly perpendicular to the incident beam through a second prism and are imaged without magnification onto slit 3, as indicated by the ray tracing in figure 4. The incident beam and slit 3 define the sampled volume. Slits 1 and 2 are fixed in position; along with movable mirrors 1 and 2 they define the particle rotation angle, 2α, through which a particle rotating in the direction indicated must turn for its reflexion to pass from slit 1 to slit 2. Since the reflexions rotate twice as fast as the particles, the slits define an actual angle of 4α. The maximum height of these slits in this apparatus is 5 cm, limited by the size of the photomultiplier

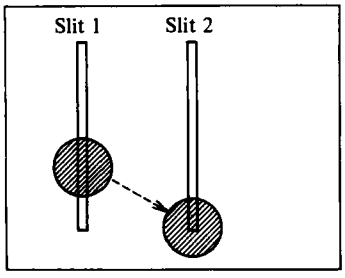

FIGURE 5. Possible positions of reflected diffraction spot relative to slits, illustrating its truncation.

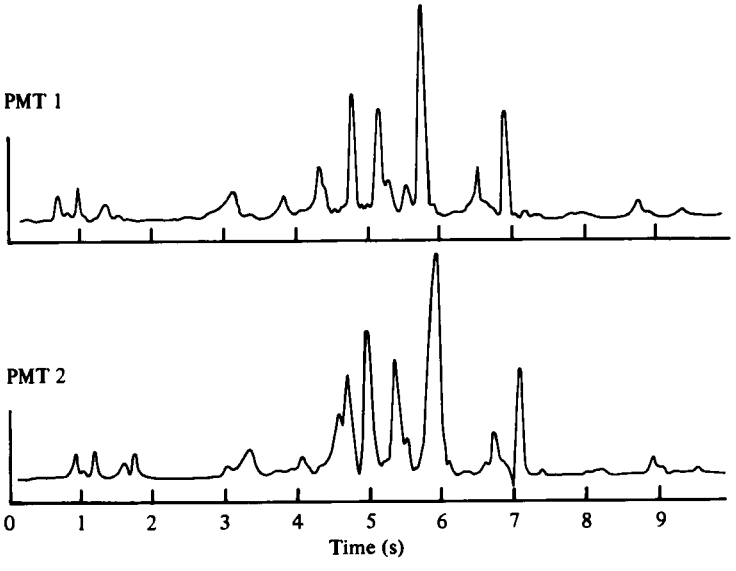

FIGURE 6. Segment of dual-channel chart recorder trace showing output of photomultipliers due to reflexions from particles embedded in a rigidly rotating rod.

anodes placed directly behind them. Consequently, only about 4 % of the total number of reflexions are intercepted by the optics. A more elaborate apparatus with specially shaped slits and larger detectors could increase the collection efficiency substantially. All of the optical components are movable, as shown by the double-headed arrows in figure 4, to allow repositioning of the sampled volume without significantly changing the reflexion path length of 37 cm or the rotation angle 2α.

(ii) *Properties of the reflexions.* Reflexions of parallel illumination from perfect mirrors, approximated by disks of radius L, are diffraction broadened to Airy disk patterns with the central disk spreading at an angle $\beta = 1{\cdot}22\lambda/2L$. For the probe mirrors $\beta \sim 1{\cdot}5°$. For an incident beam intensity I, the reflected power is $I\pi L^2$. The observed irradiance on a plane a distance z from the mirror is

$$I_r = I\pi L^2/[\pi(\beta z)^2] = 2{\cdot}69IL^4/\lambda^2 z^2. \tag{2.6}$$

Thus the intensity of the reflexion varies with the fourth power of mirror size. Additional variations can arise from the following factors: (1) particles move through an incident

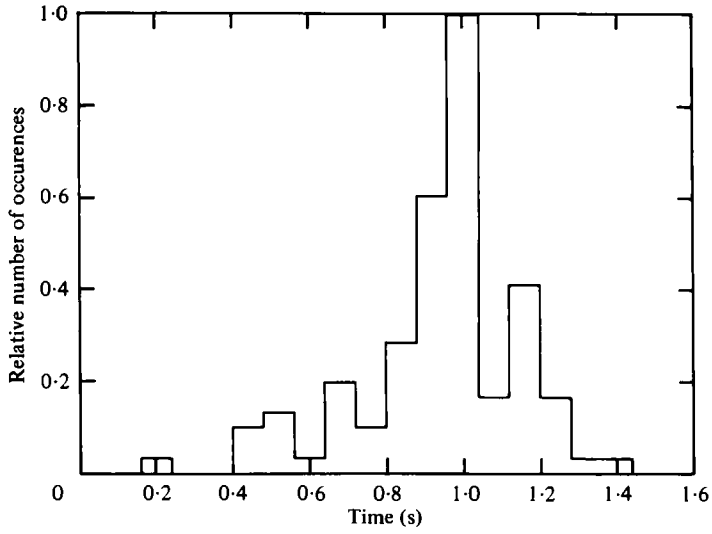

FIGURE 7. Distribution of elapsed times between threshold crossings of detector 1 followed by detector 2, as determined from data like that of figure 6.

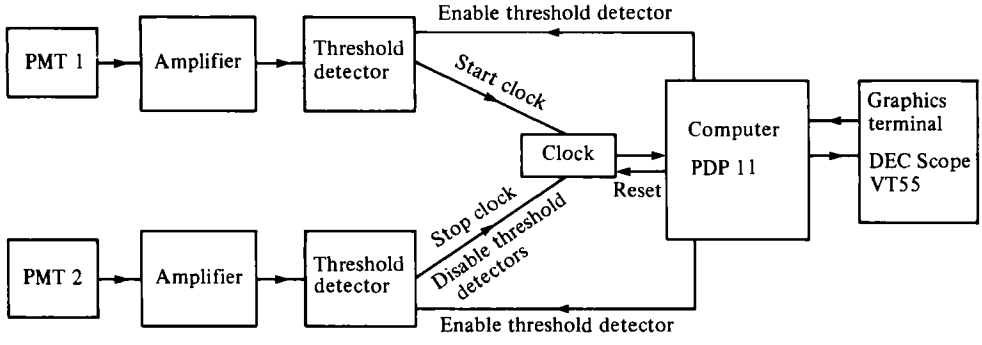

FIGURE 8. Block diagram of data analysis system.

beam with a gaussian intensity profile while they rotate, thus changing reflexion intensity; (2) as shown in figure 5, portions of the reflected beam may be cut off by the top or bottom of a slit; (3) the intensity of the ideal reflexions is angle dependent; (4) mirror imperfections as well as differences in mirror diameter vary the intensity between particles; and (5) optical screening by separate particles can attenuate the reflexion.

To characterize the reflexions a dummy specimen consisting of particles imbedded in a rigid rod of polymethylmethacrylate was rotated in the illuminating beam at one revolution per minute. Figure 6 is a segment of a dual-channel chart recorder trace of the output of the two photomultipliers recording these reflexions. The upper trace is PMT1 and the lower is PMT2. Examination of this figure shows that the amplitudes and shapes of pulses from different particles can vary substantially, and frequently the individual pulses comprising a pair differ from each other.

As shown in appendix A, the result of these variations is an uncertainty in the

measurement time between the pulses detected using a threshold detection criterion. This 'pulse variation' error can be minimized by maximizing the separation in time of the two pulses relative to their width, that is by maximizing the rotation angle α and minimizing the diffraction width β, or maximizing the ratio α/β. A narrow pulse width is achieved by the use of a short wavelength of light, for which a He–Cd laser (Liconix Model 401, $\lambda = 4431$ Å) was chosen. The optimum rotation angle is difficult to determine because all of the deleterious variations become more pronounced as the rotation angle increases and disappear at zero rotation angle. Thus there is a trade-off between maximum time separation and minimum shape variation. In practice choosing $\alpha/\beta \sim 1$ proved to be satisfactory. The measured elapsed time distribution for a constant rotation rate of the dummy specimen is plotted in figure 7. This distribution eventually determines the vorticity measurement resolution to be discussed in § 3.

(*b*) *Electronics*

A block diagram of the data acquisition system is shown in figure 8. Threshold detectors are employed to determine the time of occurrence of the pulses. A pulse from PMT1, after amplification, triggers a threshold detector, starting a clock which is accurate to 1 μs. A similar event in the second channel stops the clock and disables the threshold detectors. The elapsed time is read by an on-line computer which then resets the clock and threshold detectors, and subsequently operates on the data. To suppress low-vorticity noise, discussed in § 3 below, the system automatically resets after a predetermined elapsed time if no pulse is presented to the *off* detector. The data are converted to vorticity in the computer and displayed on a graphics terminal. Note that measurements of vorticity of only one algebraic sign are recorded with this system as described. Both signs could, however, be simultaneously recorded with duplicate electronics in which the *on* and *off* channels are interchanged.

3. Analysis of system characteristics

The precision and accuracy of vorticity measurement, data acquisition rate, temporal resolution, spatial resolution associated with the fluid volume sampled, and the background noise spectrum characterize the vorticity measurement system. These properties are closely interrelated and may be optimized selectively to suit various applications.

A special requirement of the optimization procedure is the selection of conditions that facilitate convenient separation of the measured vorticity spectrum from the characteristic background noise of the VOP system, which is unique in that the noise spectrum depends on the vorticity (signal) spectrum as well as instrumental parameters. Below, in § 3.1, expressions describing the data rate and spatial and temporal resolutions are derived, the background noise is discussed in detail, and a simple demonstration of the optimization technique is presented.

Section 3.2 describes the experimental resolution which can be expected after optimization. A system resolution function combining the effects of flow inhomogeneities and optical variations is developed to facilitate analysis of experimental results.

3.1. *Data rate and noise analysis*

(*a*) *Data rate.* Assume a sampled volume of cross-sectional area A and uniform length s, a mirror concentration n, flow at mean velocity v, and a vorticity vector $(\omega_1, 0, 0)$. The rate at which mirrors enter and pass through the sampled volume is nAv, of which a small fraction, f, will present the proper vertical orientation to reflect light in the direction of slits 1 and 2, which are positioned to measure the x component of vorticity. Thus the effective mirror passage rate is $R_p = nAvf$. The particles rotate through an angle $\phi = \frac{1}{2}(s/v)\,\omega_1$ while they transit the sample volume. Those that rotate through the appropriate azimuth defined by slit 1 and continue through an additional angle 2α before leaving the sampled volume can generate vorticity data.

The temporal resolution associated with an individual datum is the time for rotation through 2α, that is $\tau_1 = 4\alpha/\omega_1$. Ideally $\alpha \to 0$ would yield instantaneous data. In this limit the probability of a mirror entering the sampled volume with an initial azimuth suitable for data production is $\phi/2\pi$, yielding an ideal limiting data rate $R_i = 2R_p\phi/2\pi$ (see appendix B), or

$$R_i = fnAs\omega_1/2\pi = fN\omega_1/2\pi, \tag{3.1}$$

where N is the average number of mirrors within the sampled volume. R_i is also the limiting data rate generated by a mirror density n as the flow velocity vanishes, or $\phi \to \infty$. The mirrors rotate at a frequency $\omega_1/4\pi$ with a fraction f oriented to produce two data per rotation, due to the twofold symmetry of the mirrors.

To measure a rotation time the detector slits 1 and 2 must be separated; hence α is necessarily non-zero. Consequently, at non-zero flow velocity, some mirrors enter the sampled volume with an azimuth which will not allow data generation during their residence time. A mirror may then generate pulses which either trigger the *on* detector and the *off* detector in sequence, producing a 'valid' datum, trigger only one detector, or trigger no detector before leaving the sampled volume. Appendix B enumerates these possibilities and shows that mirrors having an initial azimuth suitable for valid data production are detected at a rate

$$\left.\begin{aligned} R_a &= fnAv(\phi - 2\alpha)/\pi, && (\phi - 2\alpha) > 0, \\ R_a &= 0, && (\phi - 2\alpha) < 0. \end{aligned}\right\} \tag{3.2}$$

The rate at which the individual detectors are triggered, however, remains equal to R_i, independent of α and v. The difference, $R_r = R_i - R_a$, defines the rate at which pulses appear in each detection channel that have no correlated pulses (those due to the same reflexion) in the other channel. These 'random' pulses result in a further reduction of the measured data rate by occasionally appearing between the two correlated or 'valid' pulses comprising the 'valid on–off pair' required to generate a valid datum. Random pulses occurring sequentially in the two channels may also produce 'false' data values, resulting in 'background noise'.

The measured valid data rate, R_m, is determined by enumeration of the possible sequences of events involving valid and random pulses. Five such sequences can occur:

(1) A valid on–off pair is uninterrupted and produces a valid datum.

(2) A valid pulse starts the clock and a random pulse stops it, generating noise.

(3) A random pulse starts the clock and a valid off pulse stops it, generating noise and disqualifying the valid pair from data production.

(4) Random pulses both start and stop the clock, generating noise.

(5) Two (or more) valid on–off pairs overlap, disqualifying the second pair from data production.

Sequences 2, 3 and 5 limit the measured data rate to some value less than R_a. In addition, sequences 2, 3 and 4 generate invalid elapsed-time measurements, thus creating a spectrum of false vorticity noise.

The measured data rate then is

$$R_m = R_a - R_2 - R_3 - R_5, \tag{3.3}$$

where R_j are the rates at which the enumerated sequences $j = 2, 3, 5$ occur. These rates are calculated in appendix C with the results

$$R_2 = R_a[1 - \exp(-4\alpha R_r/\omega_1)], \tag{3.4a}$$

$$R_3 = R_a R_r/(R_r + R_i), \tag{3.4b}$$

$$R_5 = R_a[1 - \exp(-4\alpha R_a/\omega_1)]. \tag{3.4c}$$

On inserting these results in (3.3), the measured data rate becomes

$$R_m = R_a[\exp(-4\alpha R_r/\omega_1) + \exp(-4\alpha R_a/\omega_1) - (2R_r + R_i)/(R_r + R_i)]. \tag{3.5}$$

(*b*) *Noise.* Sequences 2, 3 and 4 above yield continuous distributions of values of the elapsed time. Since these are all Poisson processes (appendix C), the probability density of elapsed times is directly calculable. Weighting the probability densities with the corresponding noise generation rates yields the total elapsed-time noise distribution:

$$D_n(t_n) = [R_r R_i^2/(R_r + R_i)]\exp(-R_i t_n) + \begin{cases} R_a R_r \exp(-R_r t_n), & t_n < 4\alpha/\omega_1, \\ 0, & t_n > 4\alpha/\omega_1. \end{cases} \tag{3.6}$$

The first term is generated by sequences 3 and 4, and the second term is by sequence 2. This distribution determines a fictitious vorticity distribution, or vorticity noise spectrum, conveniently written as

$$B_n(\omega_n) = [4\alpha(R_i - R_a)/\omega_n^2][\exp(-4\alpha R_i/\omega_n)] \times [R_i^2/(2R_i - R_a) + \begin{cases} R_a \exp(4\alpha R_a/\omega_n)], & \omega_n > \omega_1, \\ 0], & \omega_n < \omega_1. \end{cases} \tag{3.7}$$

This distribution has a sharp peak at $\omega_n(\text{peak}) = 2\alpha R_i$, and a long tail towards high values of vorticity. The total noise data rate is

$$R_n = (R_i^2 + R_i R_a - R_a^2)/(2R_i - R_a) - R_a \exp[-4\alpha(R_i - R_a)/\omega_1]. \tag{3.8}$$

(*c*) *Discussion and optimization.* The measured data rate given by (3.5) is implicitly a function of all experimental parameters, $R_m = R_m(f, N, \alpha, s, v, \omega_1)$. The VOP system is optimized by maximizing the data rate for a particular experimental vorticity value and spatial resolution. The spatial resolution s^{-1} is limited by the requirement that the mirrors have sufficient residence time in the sampled volume to rotate through the angle 2α before translating out of the sampled volume, that is, $R_a \geqslant 0$, or by (3.2)

$$\omega_1/v \geqslant 4\alpha/s. \tag{3.9}$$

The data rate is limited by overlapping pulse pairs if the flow velocity is small, and by the requirement that the true vorticity peak be easily distinguished from the noise spectrum if operating near the vorticity/velocity threshold limit given by (3.9). Since both the data rate and the noise spectrum depend on the number of mirrors within the sampled volume, optimization generally imposes a condition on N. Examination of equations (3.5) and (3.7) in the limits $v \to 0$ and $\omega_1/v \to 4\alpha/s$ illustrate these limitations.

(i) *Zero flow velocity limit.* Since $R_r \to 0$ and $R_a \to R_i$ as $v \to 0$, (3.5) shows that

$$\lim_{v \to 0} R_m = R_i \exp(-4\alpha R_i/\omega_1). \tag{3.10}$$

This data measurement rate peaks at $R_i = \omega_1/4\alpha$, resulting in a maximum possible data rate of

$$R_{m\,\max} = \omega_1/4e\alpha = \omega_1/10{\cdot}87\alpha. \tag{3.11}$$

Optimization of the number of mirrors in the sampled volume for this data rate requires, from (3.1),

$$N_{\text{opt}} = \pi/2fea = 0{\cdot}58/f\alpha. \tag{3.12}$$

Either more or fewer mirrors in the sampled volume will reduce the data rate.

(ii) *Vorticity threshold limit.* In the vorticity measurement threshold limit, $\omega_1/v \to 4\alpha/s$, the valid pulse pair rate $R_a \to 0$ and $R_n \to R_i$, so that all of the pulses eventually become random, and the vorticity peak vanishes into the noise background. Appropriate approximations of (3.5) and (3.7) provide an analysis of the approach to this limit.

The background noise spectrum at $\omega_n = \omega_1$ here becomes

$$B_n(\omega_1) \simeq 2\alpha R_i^2/\omega_1^2 = \tfrac{1}{2}\alpha(fN/\pi)^2, \tag{3.13}$$

where the assumption $2fN\alpha/\pi \ll 1$ has been invoked to approximate the exponential in (3.7) by unity. Equation (3.5) becomes, approximately,

$$R_m \simeq (fN/2\pi)(\omega_1/2 - 2\alpha v/s). \tag{3.14}$$

Assuming that the valid data peak at ω_1 is actually spread over a width $\delta\omega$, the spectral density of the valid data is $R_m/\delta\omega$ so that a 'signal to noise' ratio can be defined as

$$r_n = (R_m/\delta\omega)/B_n(\omega_1) = \pi(\omega_1/2 - 2\alpha v/s)/\alpha f N\delta\omega. \tag{3.15}$$

Selection of a signal-to-noise ratio r_n as large as desired specifies a maximum value of N,

$$N \leqslant \pi(\omega_1/2 - 2\alpha v/s)/\alpha f r_n \delta\omega. \tag{3.16}$$

With the maximum value of N, the noise peak occurs at

$$\omega_n(\text{peak}) = 2\alpha R_i = \omega_1(\omega_1/2 - 2\alpha v/s)/r_n\delta\omega. \tag{3.17}$$

If $\omega_1/\delta\omega \ll 1$ then $\omega_n(\text{peak}) \ll \omega_1$ and the false peak is clearly separated from the real peak, as desired. These results are graphically illustrated in figure 9 where the valid peak is represented by a gaussian of width $\delta\omega$, $r_n = 20$, N is determined by (3.15) and the other experimental parameters are chosen to correspond to actual experiments.

(iii) *General case.* The entire discussion of data rate and noise has, to this point, assumed a single value (or narrow range) of the vorticity vector, enabling this comprehensive illustration of optimization. However, real flow fields may have a distribution of vorticity vectors spread out in magnitude and containing components other than the one which is sampled. In such situations the values of R_i and R_a are still proportional to the mirror density n, but quantitative analysis becomes excessively tedious. However, the preceding discussion suggests that the true vorticity spectrum can always be separated from the noise spectrum by reducing the particle concentration until the peak of the noise spectrum is located at a value of vorticity which is much

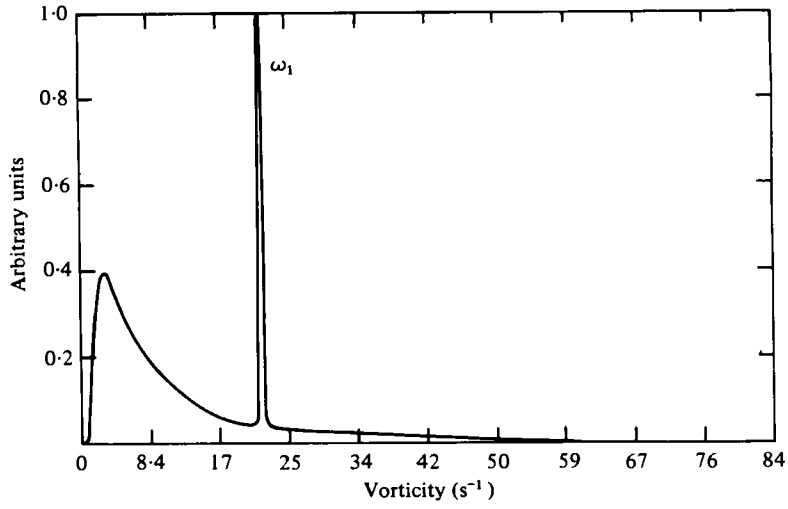

FIGURE 9. Theoretical noise distribution near vorticity/velocity threshold value.

less than the threshold value of measurable vorticity, $\omega_{\min}$, for the particular flow situation. This peak is easily recognized but it can be suppressed by automatically resetting the detectors after a time interval t_r has elapsed after an *on* pulse without an *off* pulse. Choosing t_r so that $4\alpha/\omega_{\min} \ll t_r \ll 1/R_i$ allows a slight increase in the measured data rate, and a considerable improvement in the appearance of the vorticity distribution by suppressing the low-vorticity noise.

3.2. *Vorticity resolution*

Vorticity measurement uncertainties limit the vorticity resolution of the VOP system and broaden measurements of vorticity distributions. Limitations of optical geometry and imperfection of the probe particle reflexions introduce small errors in all reflexion transit time measurements and thus in vorticity measurements, whatever the flow system. In addition finite spatial resolution in the presence of a macroscopic spatial vorticity gradient broadens the vorticity distribution. In order to describe the properties of the VOP system, a vorticity resolution function is defined. It consists of a convolution of an optical resolution function g_o and a function g_v due to vorticity gradients. The contribution of noise is ignored in the theoretical analysis presented here.

(*a*) *Optical resolution*

An experimental estimate of the optical resolution in the absence of a vorticity gradient is obtainable from the simulation vortex experiment described in § 2.4 (*a*) (ii). The measured time delay distribution shown in figure 7 can be inverted to obtain the measured optical resolution shown in figure 10. This experiment determines the optical resolution function $g_o(\omega/\omega_1)$ of the present VOP system for a vorticity spike at ω_1. It displays a smooth optical resolution function peak with a root-mean-square vorticity resolution of about 9 %. Since this experiment suffers from a small vorticity/velocity ratio away from the axis of rotation, it is not surprising that a broad low-level tail at higher vorticity appears. It is a combination of the pulse variation error

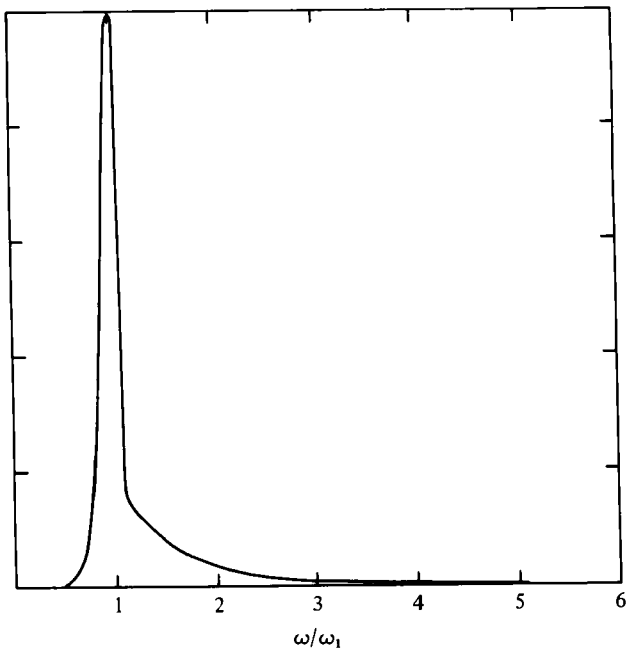

FIGURE 10. Experimentally determined optical resolution function.

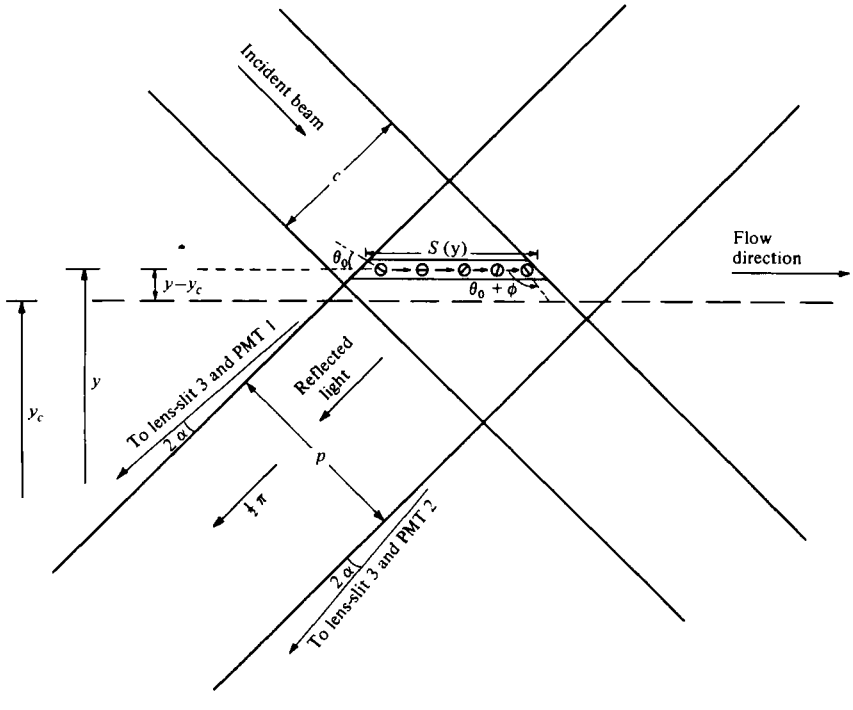

FIGURE 11. Notation for analysis of sampled volume.

Limits (valid for $y > 0$, $d > c$)	$s(y)$
$(d-c)/2\sqrt{2} > (y-y_c) > -(d-c)/2\sqrt{2}$	$\sqrt{(2)}\,c$
$(d+c)/2\sqrt{2} > (y-y_c) > (d-c)/2\sqrt{2}$	$\sqrt{(2)}\,c-2[y-y_c-(d-c)/2\sqrt{2}]$
$-(d+c)/2\sqrt{2} < (y-y_c) < (d-c)/2\sqrt{2}$	$\sqrt{(2)}\,c+2[y-y_c+(d-c)/2\sqrt{2}]$

TABLE 1

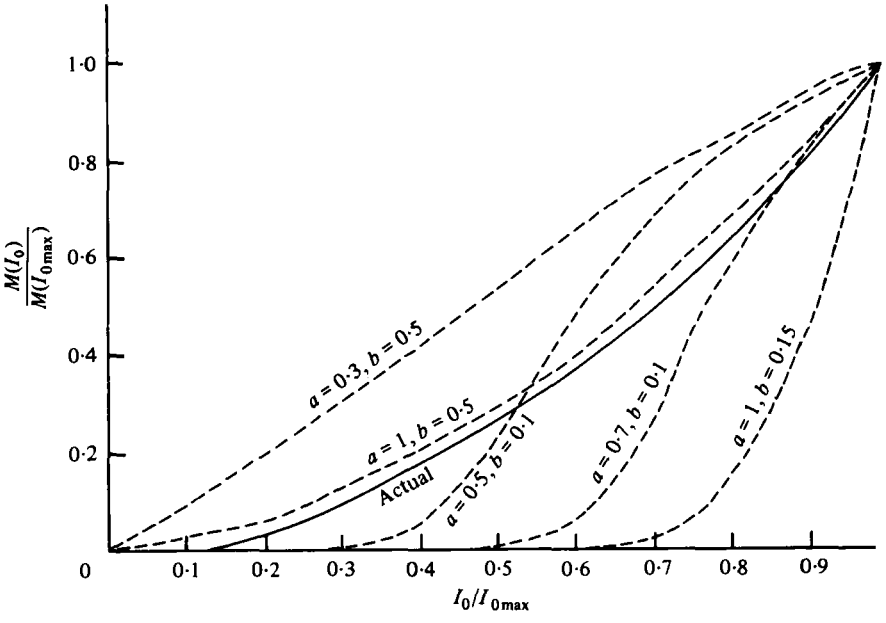

FIGURE 12. Theoretical and experimental pulse detection rates as a function of intensity, used to determine the reflexion intensity distribution.

discussed in appendix A and the false data background discussed in the previous section. Note that the pulse variation error, as well as the noise, increases in magnitude as $\phi \to 2\alpha$ since the particles translate through a larger segment of the gaussian incident intensity profile. This means that the accuracy of the data improves as ω/v increases, and that the relative magnitude of the tail will depend on ω/v.

(b) Vorticity gradient resolution

The measured vorticity distribution in a system with non-uniform vorticity is determined primarily by the size and shape of the sampled volume, and the vorticity and velocity gradients. For the optical geometry shown in figure 11 the sampled volume is a rectangular box oriented at 45° relative to a flow channel. The length s varies with position. Calling y the co-ordinate relative to the centre of the channel and y_c the position of the centre of the sampled volume relative to the centre of the flow channel, then the length at position y, $s(y, y_c, c, d)$ has the values summarized in table 1, where c is the width of the incident beam and d the width of slit 3. The local contribution to

the data rate, now a function of y, is approximated by (3.2) with the assumption that the effects of random pulses and overlapping valid pulse pairs are negligible. Thus

$$R_a = R_a[\phi(\omega(y, y_c), v(y, y_c), s(y, y_c, c, d))] = fnAv(\phi - 2\alpha)/\pi, \quad \phi > 2\alpha, \tag{3.18}$$

where the function $\phi(\omega)$ is the angle through which a particle rotates during its transit of the sampled volume, defined in § 3.1 (*a*). A measurement of vorticity with the sampled volume centred at point y_c will now result in a vorticity distribution $g_v(w, v, c, d)$, where $g_v \propto R_a$. This piece of the resolution function is called the vorticity-sampling function.

(*c*) *Optically corrected sampling function*

The non-uniformity of the illuminating laser beam and the distribution of probe particle reflecting power couple in a curious fashion. The illumination is non-uniform because the laser beam has a gaussian intensity profile. Since larger probe mirrors reflect more strongly than small mirrors they trigger the threshold reflexion detectors at lower illumination intensities and thus are observable farther out into the fringes of the illuminating beam.

Defining $m(I)\,dI$ as the number of additional reflexions that will become detectable as the incident intensity increases from I to $I + dI$, the total number of mirrors with reflexions bright enough to be detectable is $\int_0^{I_0} m(I)dI$ if the maximum incident intensity is I_0. Defining the intensity-dependent beam width, $c = c(I)$, the numberof single channel reflexions detected per unit time is

$$M = B\int_0^{I_0} c(I)\, m(I)\, dI, \tag{3.19}$$

where B is some constant. For a gaussian laser beam of width c_0 at $I/I_0 = e^{-2}$ the beam width between points of intensity I is $c(I)/c_0 = (\frac{1}{2}\ln(I_0/I))^{\frac{1}{2}}$ so that

$$M(I_0) = c_0 B\int_0^{I_0} (\tfrac{1}{2}\ln(I_0/I)^{\frac{1}{2}}\, m(I)\, dI. \tag{3.20}$$

Fitting $m(I)$ to a gaussian function for simplicity yields

$$M(I_0) = c_0 B\int_0^{I_0} (\tfrac{1}{2}\ln(I_0/I))^{\frac{1}{2}} \exp[-(I/I_0 - a)^2/2b^2]\, dI. \tag{3.21}$$

Figure 12 shows several scaled curves of $M(I_0)$ *vs.* I_0 with various values of a and b. Actual data, obtained by counting the number of pulses triggering threshold detector 1 in a fixed period of time for various attenuations of the incident beam, most closely fits the curve with $a = 1$, $b = 0{\cdot}5$. The vorticity gradient function g_v can now be adjusted to $g_v'(\omega, y_c, c_0, d)$ to account for the variations in probe particle reflecting power by performing the integral

$$g_v'(\omega, y_c, c_0, d) = \int_0^{I_0} g_v[\omega, y_c, c(I), d]\, m(I)\, dI. \tag{3.22}$$

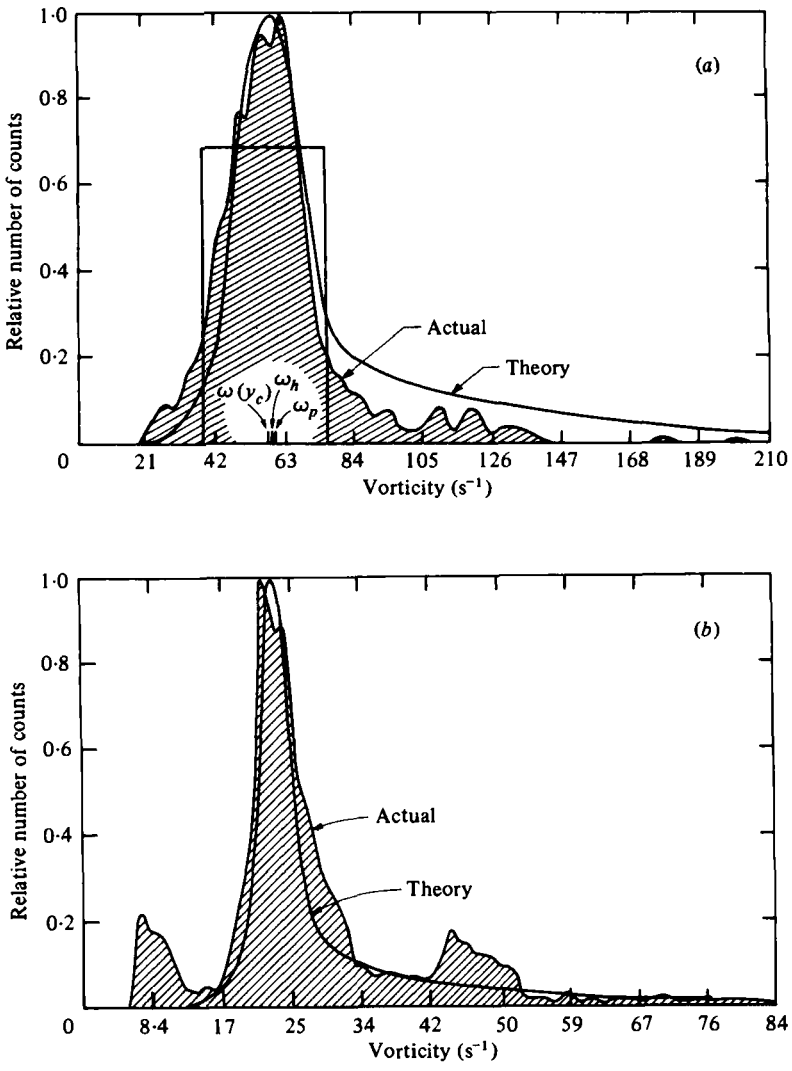

FIGURE 13. Superposition of vorticity resolution function and measured distribution. Flow parameters: (*a*) $w = 0{\cdot}22$ cm, $y_c = 0{\cdot}157$ cm, $c_0 = 0{\cdot}1$ cm, $d = 0{\cdot}1$ cm, $v_0 = 8{\cdot}65$ cm s^{-1}, (*b*) $w = 0{\cdot}8$ cm, $y_c = 0{\cdot}74$ cm, $c_0 = 0{\cdot}1$ cm, $d = 0{\cdot}1$ cm, $v_0 = 10{\cdot}3$ cm s^{-1}.

(*d*) *Vorticity resolution function*

The complete vorticity resolution function $g(\omega, y_c, c_0, d)$ is the convolution of the corrected sampling function g_v' with the measured optical resolution function g_o. Thus the vorticity resolution function is

$$\left.\begin{aligned} g(\omega, y_c, c_0, d) &= \int_0^\infty d\omega_a\, g_v'(\omega_a, y_c, c_o, d)\, g_o(\omega/\omega_a) \\ &= \int_0^\infty d\omega_a\, g_o(\omega/\omega_a) \int_0^{I_0} dI\, g_v(\omega_a, y_c, c(I), d) \exp[-2(I/I_0 - 1)^2]. \end{aligned}\right\} \quad (3.23)$$

(e) *Illustrative calculation of vorticity resolution function*

The simple example of laminar two-dimensional, Poiseuille flow (Batchelor 1967, § 4.2) illustrates the calculation of the vorticity resolution function. The velocity and vorticity profiles are for this case

$$v(y) = v_0(1-y^2/w^2), \quad \omega(y) = 2v_0 y/w^2, \tag{3.24), (3.25}$$

where v_0 is the velocity at the centre of the channel and w is the channel width. The angle of particle rotation during transit of the sampled volume is

$$\phi(y, y_c, c, d) = s(y, y_c, c, d)\, y/(w^2-y^2). \tag{3.26}$$

The local data rate within the sampled volume is

$$R_a = (fnv_0 h\, dy/\pi)\,(1-y^2/w^2)\,[sy/(w^2-y^2)-2\alpha], \tag{3.27}$$

where $h\,dy$ is the cross-sectional area. Treating y as a function of vorticity, the vorticity-sampling function is

$$g_v(\omega, y_c, c, d) = s[y(\omega), y_c, c, d]\, y(\omega) - 2\alpha[w^2 - y^2(\omega)]. \tag{3.28}$$

Now the vorticity resolution function $g(\omega, y_c, c_0, d)$ can be calculated since all of its components are determined. The bold lines in figures 13 (a, b) show the results of numerical calculations of $g(\omega(v_0, w), y_c, c_0, d)$ from (3.22) for the present VOP system with the parameters v_0, w, y_c, c_0 and d indicated in the figure caption. For this high-symmetry geometry ($c_0 \simeq d$) the vorticity distribution is nearly symmetric, except for the noise tail. Therefore several convenient measures of the position of the vorticity peak nearly coincide, namely the putative vorticity at the centre of the measuring volume $\omega(y_c)$, the peak vorticity ω_p, and the mean of the half-maximum points ω_h.

4. VOP system test

4.1. *Test system*

Laminar, two-dimensional Poiseuille flow provides a suitable, stringent test of the reliability of the new vorticity measurement system. A Plexiglas channel, 5·1 cm high, 1·3 cm wide, and 50 cm long was constructed for this purpose. An extra piece of Plexiglas, 5·1 cm high and 25 cm long, can be inserted to reduce the channel width to a nominal 0·4 cm. A gravity-fed, recirculating pumping system drives the fluid, dibutyl phthalate, through the free-surfaced channel. Screens placed in the entrance region smooth out gross flow irregularities. Flow velocity maxima were determined by measuring the transit times of visible particles between fiducial marks. The flow system has provisions to vary all of the parameters entering into the resolution function of § 3, to facilitate its use for testing and calibrating the VOP system and determining its vorticity resolutions. A cylindrical lens placed in the path of the incident beam can change the otherwise cylindrical sampled volume into a rectangular parallelepiped.

Flow visualization was used to determine the areas within the channel where the flow is sufficiently well developed for good measurements. Suspended guanine platelets (Kalliroscope Corporation product AQ-1000) are aligned by the flow in the direction of the maximum shear rate, making boundary layers and flow inhomogeneities clearly visible. The velocity and vorticity profiles become fully developed slightly downstream

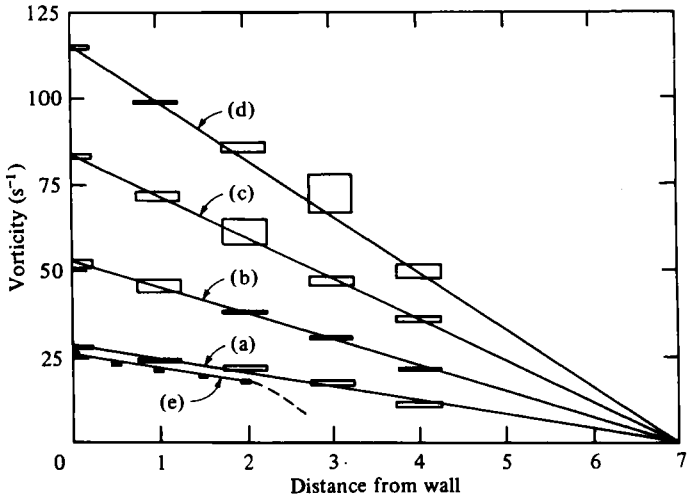

FIGURE 14. Measured vorticity profiles in Poiseuille flow. Calculated speeds: (*a*) 2·9 cm s^{-1}; (*b*) 4·8 cm s^{-1}; (*c*) 8·6 cm s^{-1}; (*d*) 13·0 cm s^{-1}; (*e*) 10·3 cm s^{-1}.

of the point at which the boundary layers from either side of the channel meet. In the 0·4 cm wide channel, observations show that this occurs at positions at least 20 cm downstream of the entrance. In the 1·3 cm wide channel it was not clear that the Poiseuille flow developed fully for velocities above 3 cm s^{-1}. Effects of the bottom of the channel appeared to be negligible above 2·5 cm. Velocities at the centre of the channel range from about 1 to 15 cm s^{-1}.

4.2. *Vorticity distributions*

Figure 13 (*a*) compares an anticipated vorticity distribution calculated in § 3 with the corresponding measured distribution using the same flow parameters in the narrow channel. The agreement is quite good, especially near the half-maximum points. The noise and pulse variation errors for this flow are apparently less significant than in the simulation vortex experiment of § 2.4 (*a*) (ii), as indicated by the differences in the tail heights. Figure 13 (*b*) shows a similar comparison of some wide-channel data taken near the channel wall. Note that the wide channel has a shallower vorticity gradient than the narrow channel, with a correspondingly narrower sampling function as expected. It also has a smaller vorticity/velocity ratio, which is responsible for the increased experimental tail amplitude and the small noise peak at low vorticity values. This distribution can be compared to the theoretical noise distribution of figure 9. The automatic reset circuit is responsible for the sharp cut-off at the low end of the experimental distribution. The experimental wide-channel data shows a curious secondary peak centred at approximately twice the value of the primary peak which appears only in observations close to the wall. It may be the result of some sort of flow fluctuations. The Reynolds number ($v_0 w/\nu$) for this flow is about 100.

A numerical device which is useful to compare different vorticity distributions is demonstrated by the rectangle drawn in figure 13 (*a*). The width and position of this rectangular construction are determined to yield the second and third moments of the

experimental distribution around its average. The bottom 10 % of the distribution is ignored in calculating the moments to eliminate the contributions of the various errors.

(*a*) *Vorticity profiles*

Several sets of vorticity measurements are plotted as functions of measurement position y_c in figure 14. They show, within error limits, the anticipated linear vorticity profiles for these Poiseuille flows, (3.25). Each vorticity point is plotted as a rectangle with a width representative of the positional uncertainty and a height equal to the difference between two measures of vorticity, namely the peak vorticity ω_p and the average of the half-maxima ω_h. In accord with § 3.2 (*d*), ω_p and ω_h should very nearly coincide with the vorticity at the centre of the sampled volume, $\omega(y_c)$. The experimental values of ω_h are repeatable to within a few per cent and are thus good measures of $\omega(y_c)$. The r.m.s. value of the differences $\omega_p - \omega_h$ provide a practical measure of the uncertainties of vorticity measurements. For these data the relative uncertainty of vorticity is about 8%.

The velocities indicated in figure 14 are calculated from the slopes of the straight lines determined by the vorticity measurements, since this measure is more precise than the flow velocity estimates. The calculated velocities do agree with the approximate measured velocities.

In the wide channel the flow has not reached a fully developed Poiseuille parabolic velocity profile. Boundary-layer theory (Landau & Lifshitz 1959, ch. 4) shows that the boundary layer 20 cm downstream from the edge of a flat plate will have a width of about 0·5 cm when the flow velocity is 10 cm s^{-1} and kinematic viscosity is 0·15 cm^2 s^{-1}. Thus there should be a high-vorticity boundary layer with small vorticity gradient near the wall that drops rapidly to zero near the edge of the boundary layer. The wide-channel vorticity profile, line (*e*) in fig. 14, appears to have a fully developed flow profile near the wall for a channel width of 1·6 cm at the correct centre-line velocity of 10·3 cm s^{-1}. However the actual channel width is only 1·3 cm and the vorticity drops sharply below the detectable minimum beyond 0·25 cm from the wall. These results are consistent with the above calculations and with the flow visualization observations that a distinct boundary layer remains.

(*b*) *Distribution widths*

Poiseuille flow allows a very simple comparison to be made between the expected vorticity resolution and the actual width of the distribution. According to equation (3.25), if a width, Δy, of the vorticity profile is uniformly sampled (s = constant), then the corresponding width $\Delta\omega$ of the vorticity distribution is

$$\Delta\omega = (2v_0/w^2)\,\Delta y. \tag{4.1}$$

In the present experiment (4.1) should provide a reasonable approximation even though s varies. Figure 15 shows a plot of mean values of $\Delta\omega$ for each of the lines in figure 14 *vs.* $2v_0/w^2$ and a straight line fit for comparison with Δy determined by (4.1). Here $\Delta\omega$ is chosen as the width of the rectangular construction discussed above. The resulting value for Δy, $\sim$ 0·1 cm, agrees with the value determined by the apparatus optics.

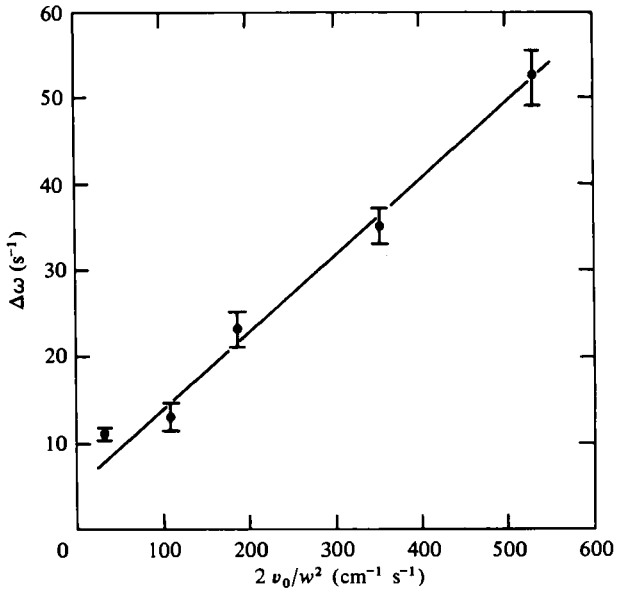

FIGURE 15. Experimental vorticity distribution widths as a function of flow parameter. Slope = 0·09 cm.

5. Summary

A system for vorticity measurement by direct optical probe has been described and tested under the stringent conditions imposed by laminar flows. The accuracy, vorticity resolution, data rate and spatial resolution of the VOP and the experimental parameters on which these properties depend have been analysed and demonstrated by the measurements with a rather primitive apparatus.

There are some fundamental interdependent limits on the VOP system capabilities. The drift velocity/vorticity ratio sets a lower limit on the spatial resolution, $s_{\min} = 4\alpha v/\omega$, since the residence time of a probe particle within the sampled volume must exceed the vorticity detection time. An upper limit on the number of particles within the sampled volume with zero flow velocity, $N_{\text{opt}} = 0{\cdot}58/f\alpha$, is determined by maximizing the data rate while requiring that reflexions from multiple particles have a small probability of overlapping. The factor f represents the geometrical data collection efficiency, which may be improved by more elaborate optical design. The maximum data acquisition rate, $R_{m\,\max} = \omega/10{\cdot}87\alpha$, is achieved in a zero flow velocity situation if the number density is determined N_{opt}. As the flow velocity increases from zero the maximum data rate decreases and background noise increases. The signal to noise ratio, $r_n \approx \pi(\frac{1}{2}\omega - 2\alpha v/s)/\alpha f N\delta\omega$ can be made as large as desired for any value of vorticity greater than the limiting value of $\omega = 4\alpha v/s$ by selecting a sufficiently small mirror number density, thus separating the valid data from the background. Table 2 summarizes this discussion of limiting-system capabilities and gives the parameters of the present realization of the VOP system.

The discussion of the background noise reveals one noteworthy point. As $\alpha \to 0$ all noise disappears, the particle number density is limited only by the size of the spherical

Parameter	Typical value
(*A*) Spatial resolution	
$s_{\min} = 4\alpha v/\omega$	$\alpha = 0{\cdot}05$
	$s_{\min} = \begin{cases} 200\ \mu\ (v/\omega = 0{\cdot}1\ \text{cm}) \\ 900\ \mu\ (v/\omega = 0{\cdot}5\ \text{cm}) \end{cases}$
(*B*) Date rate	
(1) Maximum	
$R_{m\max} = \omega/10{\cdot}87\alpha$	$R_{m\max} = 1{\cdot}84\omega$
(2) Actual	
(*a*) Zero flow velocity	
$R_i = \frac{1}{2}\omega\,(fN/\pi)$	$N = 10$
	$f = 0{\cdot}04$
	$R_i = \omega/16$
(*b*) Near ω/v threshold	
$R_a = (\frac{1}{2}\omega - 2\alpha v/s)\,(fN/\pi)$	
(*C*) Signal-to-noise ratio	
$r_n = 2\pi(\frac{1}{2}\omega - 2\alpha v/s)/\alpha f N \delta\omega$	$\omega = 22\ \text{s}^{-1}$
	$v = 10{\cdot}3\ \text{cm s}^{-1}$
	$\delta\omega = 10\ \text{s}^{-1}$
	$r_n = 22$
(*D*) Vorticity resolution	
Present practical limit	$\sim 9\,\%$

TABLE 2. Present VOP system parameters.

probe particles, and the data rate is bounded by only this density limit. In the present VOP system α must be non-zero to deal with variations of the size and shape of the reflexions. The rotation angle 2α is coupled to the divergence angle of the micro-mirror reflexions by the requirement $\alpha/\beta \gtrsim 1$. However, if particles with completely uniform mirrors, preferably perfect disks, could be produced, and if the illuminating beam were converted from a gaussian to a 'top-hat' intensity profile, the vorticity could be determined by measuring the width of a single pulse peak as it transits a slit. The minimum value of α could then be determined by the temporal resolution of the electronics, and would be very close to zero. Since the vorticity resolution, discussed at length in § 3, is also coupled to the optical parameters, the illuminating-beam intensity profile, and the particle uniformity, it would also be substantially improved by better particles. Substantial improvement of all of the operational parameters can be expected in future VOP systems. Nevertheless the need for refractive index matching of fluid and particles seems inescapable.

There appear to be no substantial obstacles to measurement of vorticity spectra and spatial correlations even in turbulence although various potential capabilities of the system, particularly those applicable to turbulence, have not yet been fully established. All three components of vorticity should be simultaneously measurable by straightforward elaboration of the present VOP system. Some special properties of the vorticity field are readily accessible since positive and negative signs of vorticity components are automatically separated. The VOP can readily average vorticity distributions over large flow volumes.

We have adapted the VOP system to vorticity measurements in mixing layers, wakes and turbulent boundary layers and are proceeding to investigate grid turbulence and coherent-structure phenomena of the type analysed in recent experimental and theoretical works (Roshko 1976; Kovasznay 1978; Aref & Siggia 1980).

We gratefully acknowledge stimulating conversations with Gary Watson, Jerry Gollub, Eric Siggia, Hassan Aref, Mark Nelkin and Spahr Webb, guidance in the assembly of the mini-computer system by Jerry Gollub, initiation into the mysteries of pearl polymerization by F. Rodriguez and patient and persistent craft in the production and evaluation of the probe particles by Chad Arnold. This work was partially supported by the National Science Foundation Grant NDR-77-0031.

Appendix A

Consider the measurement of the time interval between two roughly gaussian-shaped pulses which may have truncated or very noisy tops. The noise prevents the use of a peak detector as an accurate indicator of the occurrence of an event. A threshold detector may provide more reliable data, but introduces errors if the pulse amplitudes and widths are not constant.

Assume the pulses have Gaussian shape but different width and height, with their peaks separated by a true time τ_p. The pulses are described by the equations

$$S_1(t) = A_1 \exp\left[-t^2/2\sigma_1^2\right], \tag{A 1}$$

$$S_2(t) = A_2 \exp\left[(t-\tau_p)^2/2\sigma_2\right]. \tag{A 2}$$

If the threshold detectors trigger at an amplitude a_0 the measured elapsed time is $\tau = t_2 - t_1 = \tau_p + \sigma_1(2\ln A_1)^{\frac{1}{2}} - \sigma_2(2\ln A_2)^{\frac{1}{2}}$. The fractional error is

$$\frac{\Delta\tau}{\tau_p} = \frac{\tau-\tau_p}{\tau_p} = \frac{\sigma_1(2\ln A_1)^{\frac{1}{2}} - \sigma_2(2\ln A_2)^{\frac{1}{2}}}{\tau_p}. \tag{A 3}$$

The error is minimized by maximizing τ_p and minimizing σ_1 and σ_2. If $\sigma_1 \approx \sigma_2$ and $A_1 = CA_2$, where C is a constant, then $\Delta\tau \approx \sigma_2\sqrt{(2)}\,[(\ln C + \ln A_2)^{\frac{1}{2}} - (\ln A_2)^{\frac{1}{2}}]$, which approaches zero as A_2 increases, suggesting that large pulse amplitudes are also desirable.

Appendix B

Here are derived the rates of registry of valid vorticity data and of false data due to velocity-induced rapid transits of the sampled volume, and the resulting false vorticity distribution.

Defining a co-ordinate system for mirror orientation in which the azimuthal direction to the point half-way between slits 1 and 2 is taken as $\frac{1}{2}\pi$, a mirror enters the sampled volume with azimuth θ_0 and exits at azimuth $\theta = \theta_0 + \phi$, where $\phi = \frac{1}{2}(s/v)\,\omega$. To register a valid vorticity datum it must pass through azimuths $\frac{1}{2}\pi - \alpha$ and then $\frac{1}{2}\pi + \alpha$ to trigger PMT1 (*on*) and PMT2 (*off*) in sequence (see figure 11). While traversing the sampled

Probability	$\phi < 2\alpha$	$2\alpha < \phi < 2\pi - 2\alpha$	$2\pi - 2\alpha < \phi < 2\pi$	$2\pi < \phi < 2\pi + 2\alpha$	$\phi > 2\pi + 2\alpha$
P_a	0	$\frac{\phi - 2\alpha}{2\pi}$	$\frac{\phi - 2\alpha}{2\pi}$	0‡	†
P_b	$\phi/2\pi$	$\frac{2\alpha}{2\pi}$	$\frac{2\pi - \phi}{2\pi}$	0	†
P_c	$\phi/2\pi$	$\frac{2\alpha}{2\pi}$	$\frac{2\pi - \phi}{2\pi}$	0	†
P_d	$\frac{2\pi - 2\phi}{2\pi}$	$\frac{2\pi - 2\alpha - \phi}{2\pi}$	0	0	†
P_e	0	0	$\frac{2\alpha + \phi - 2\pi}{2\pi}$	$\frac{2\alpha - \phi + 2\pi}{2\pi}$	†
P_{a+c}	0	0	0	$\frac{\phi - 2\pi}{2\pi}$	†
P_{b+a}	0	0	0	$\frac{\phi - 2\pi}{2\pi}$	†
P_{a+d}	0	0	0	$\frac{4\pi - \phi - 2\alpha}{2\pi}$	†

† When $\phi > 2\pi + 2\alpha$ substitute $\phi - 2j\pi$ for ϕ, where j is the integer indicating the number of complete revolutions that have occurred: j type-a events and one additional event must occur for each particle.

‡ Note that $P_{a+c} + P_{b+c} + P_{a+d} = (\phi + 2\alpha)/2\pi$.

TABLE 3

volume a single rotating mirror with $\phi < 2\pi$, referred to below as an event, can trigger the detectors in several possible sequences, generating the following five distinct cases.

Event	Result
(*a*) $\theta_0 < \frac{1}{2}\pi - \alpha$, $\theta > \frac{1}{2}\pi + \alpha$	good data
(*b*) $\theta_0 > \frac{1}{2}\pi - \alpha$, $\theta > \frac{1}{2}\pi + \alpha$	*off* only
(*c*) $\theta_0 < \frac{1}{2}\pi - \alpha$, $\theta < \frac{1}{2}\pi + \alpha$	*on* only
(*d*) $\theta < \frac{1}{2}\pi - \alpha$	no detection
(*e*) $\theta_0 < \frac{1}{2}\pi + \alpha$, $\theta > \frac{1}{2}\pi - \alpha$	*off* followed by *on*

If $\phi > 2\pi$ then each mirror can generate more than one event. Table 3 shows the probability of occurrences of each type of event generated by an individual mirror. P_x denotes the probability of only a type x event, while P_{x+y} denotes the joint probability of a type x event followed by a type y event.

The average rate at which type x events occur is equal to twice the mean rate ($R_p = fNAv$) at which mirrors with proper (detectable) vertical orientation flow through the sample volume times the event probability P_x,

$$R_x = 2R_p P_x, \tag{B 1}$$

except that type a events (valid data generators) occur at the rate $R_a = 2(k + P_a) R_p$, where the integer k is the number of complete rotations. The factor of 2 is a result of the rotational symmetry of the mirrors. Of interest are the observations that, for all $\phi > 2\alpha$, $R_a = R_p(\phi - 2\alpha)/2\pi$, and the rates at which all *on* (type a or c or e) and all *off* (type a or b or e) events occur equal, not surprisingly, the ideal data rate, or

$$R_{on} = R_{off} = R_i = fN\omega/2\pi.$$

Appendix C

The noise generation rates due to the various sequences of presentations of random and valid pulses are calculated here. Recall that pulses presented to the *off* detector before the clock has been started pass undetected. Similarly, pulses presented to the *on* detector while the clock is running also pass undetected.

Consider those sequences wherein random pulses presented to the *on* detector with rate R_r start the clock, and either random or valid pulses presented to the *off* detector at rate R_i stop it. The rate R_f of occurrence of false data generating pulse pairs in this case is the rate of random pulse presentations to the *on* detector, R_r, multiplied by the probability of detection of these pulses, $1/(1+R_r/R_i)$, or

$$R_f = R_r R_i/(R_i+R_r). \tag{C 1}$$

This case can be divided into two sub-cases where the *off* detector is triggered by a valid pulse, or it is triggered by a random pulse. The first has a probability R_a/R_i of occurrence, and the second has probability R_r/R_i. Hence, the rate of random-*ons* + valid-*offs* (sequence 3) is

$$R_3 = (R_a/R_i)\,R_f = R_r R_a/(R_r+R_i) \tag{C 2}$$

and the rate of random-*ons*–random-*offs* (sequence 4) is

$$R_4 = R_r^2/(R_r+R_i). \tag{C 3}$$

Random events occurring at an average rate R describe a Poisson process (Lindgren 1976). Thus, starting at an *on* detection, the normalized probability density of elapsed times until a random *off* detection is

$$P(R,t) = R\exp(-Rt), \tag{C 4}$$

where the *off* detections occur at rate R. For the cases considered above the *off* rate is, from (3.1), R_i, so $R = R_i$. The resulting elapsed time distribution, weighted by the false data rate, is $D(t) = R_f P(R_i, t)$.

Now consider sequence 2 where a valid pulse pair starts the clock and a random pulse stops it. There is an additional restriction: the random pulses must occur in the time interval $[0, 4\alpha/\omega_1]$. Thus the probability of this sequence occurring is

$$P_2 = \int_0^{4\alpha/\omega_1} P(R_r, t)\,dt = 1-\exp(-4\alpha R_r/\omega_1). \tag{C 5}$$

Since valid pulse pairs occur at rate R_a, the rate at which this source of false data is generated is

$$R_2 = R_a P_2 = R_a[1-\exp(-4\alpha R_r/\omega_1)]. \tag{C 6}$$

Finally, the probability of two valid pulse pairs overlapping (sequence 5) is

$$P_5 = \int_0^{4\alpha/\omega_1} P(R_a, t)\,dt \tag{C 7}$$

and the rate at which data is lost to this sequence of events is

$$R_5 = R_a P_5 = R_a[1-\exp(-4\alpha R_a/\omega_1)]. \tag{C 8}$$

REFERENCES

AREF, H. & SIGGIA, E. D. 1980 Vortex dynamics of the two-dimensional turbulent shear layer. *J. Fluid Mech.* **100**, 705.

BATCHELOR, G. K. 1967 *An Introduction to Fluid Dynamics.* Cambridge University Press.

CADLE, R. 1955 *Particle Size Determination.* Wiley-Interscience.

CHWANG, A. & WU, T. 1974 Hydromechanics of low-Reynolds-number flow. Part 1. Rotation of axisymmetric prolate bodies. *J. Fluid Mech.* **63**, 607.

ECKELMANN, H., NYCHAS, S. G., BRODKEY, R. S. & WALLACE, J. M. 1977 Vorticity and turbulence production in pattern recognized turbulent flow structure. *Phys. Fluids* **20**, 5225.

FOSS, J. F. 1977 The Vorcom, Part 2: Demonstration vorticity measurements. *Third Annual Report, NASA, Langley Research Center.*

FRENKIEL, F. N., KLEBANOFF, P. S. & HUANG, T. T. 1979 Grid turbulence in air and water. *Phys. Fluids* **22**, 1606.

HOPFF, H., LÜSSI, H. & GERSPACHER, P. 1964 Contribution to suspension polymerization. *Makromolekulare Chemie* **78**, 24.

JEFFREY, J. B. 1922 The motion of ellipsoidal particles immersed in a viscous fluid. *Proc. Roy. Soc.* A **102**, 161.

JOHNSON, D. H. & WEBB, W. W. 1972 *Bull. Am. Phys. Soc.* **17**, 1084. See also Johnson, D. H. 1975 Measurement of the rate of strain tensor in a turbulent flow using light scattering from asymmetric particles. Ph.D. thesis, Cornell University.

KOVASZNAY, L. S. G. 1978 Large scale structure in turbulence: A question or an answer? In *Structure and Mechanisms of Turbulence I* (ed. H. Fiedler). Lecture Notes in Physics, vol. 75. Springer.

LANDAU, L. & LIFSHITZ, E. 1959 *Fluid Mechanics.* Pergamon.

LINDGREN, B. W. 1976 *Statistical Theory*, § 3.2. MacMillan.

REDFARN & BEDFORD 1960 *Experimental Plastics: A Practical Course for Students.* Wiley-Interscience.

RODRIGUEZ, F. 1970 *Principles of Polymer Systems.* McGraw-Hill.

ROSHKO, A. A. 1976 Structure of turbulent shear flows: A new look. *A.I.A.A. J.* **14**, 1349.

TENNEKES, H. & LUMLEY, J. 1972 *A First Course in Turbulence.* Massachusetts Institute of Technology Press.

WILLMARTH, W. W. & BOGAR, T. J. 1977 Survey and new measurements of turbulent structure near the wall. *Phys. Fluids* **20**, 59.